

# In vivo brain viscoelastic properties measured by magnetic resonance elastography

Michael A. Green,<sup>1\*</sup> Lynne E. Bilston<sup>1</sup> and Ralph Sinkus<sup>2</sup>

<sup>1</sup>Prince of Wales Medical Research Institute, UNSW, Sydney, Australia

<sup>2</sup>Laboratoire Ondes et Acoustique, ESPCI, Paris, France

Received 19 June 2007; Revised 10 December 2007; Accepted 31 December 2007

**ABSTRACT:** Magnetic resonance elastography (MRE) is a non-invasive imaging technique used to visualise and quantify mechanical properties of tissue, providing information beyond what can be currently achieved with standard MR sequences and could, for instance, provide new insight into pathological processes in the brain. This study uses the MRE technique at 3 T to extract the complex shear modulus for *in vivo* brain tissue utilizing a full three-dimensional approach to reconstruction, removing contributions of the dilatational wave by application of the curl operator. A calibrated phantom is used to benchmark the MRE measurements, and *in vivo* results are presented for healthy volunteers. The results provide data for *in vivo* brain storage modulus ( $G'$ ), finding grey matter (3.1 kPa) to be significantly stiffer than white matter (2.7 kPa). The first *in vivo* loss modulus ( $G''$ ) measurements show no significant difference between grey matter (2.5 kPa) and white matter (2.5 kPa). Copyright © 2008 John Wiley & Sons, Ltd.

**KEYWORDS:** elastography; MRI; brain; viscoelastic properties

## INTRODUCTION

The mechanical properties of the brain have been examined extensively *in vitro* where postmortem and dissection degradation are likely to change its properties, but few data obtained *in vivo* exist because of the difficulty of making measurements non-invasively. The *in vivo* viscoelastic properties of the brain may also change during disease pathogenesis or aging. Magnetic resonance elastography (MRE) is an innovative imaging technique developed to non-invasively map and quantify the viscoelastic properties of tissue *in vivo* (1,2). Measurements of these properties are obtained indirectly by imaging low-frequency mechanically excited shear waves within the tissue of interest. A dynamic MRE approach is undertaken in this research in which continuous excitation at a specified frequency creates a steady-state wave in the medium. Previous studies (3–6) have shown that the localised properties of the tissue affect the motion of the traversing wave (i.e. local amplitude and phase), and subsequent reconstruction of the shear elasticity and shear viscosity can be achieved.

MRE has been used as a tool to image and assess tissue properties in several areas of the body such as breast tissue (7–9), prostate (10) and skeletal muscle (11,12). A change in elasticity can often represent a pathological change in the tissue and provide information for

diagnostic assessment (13). Properties of brain tissue have not been well quantified *in vivo*, and only a few experimental studies have measured tissue properties in different areas of the brain. There have been some recent investigations using the MRE technique to quantify grey and white matter stiffness within the brain (14–17), but there have been no *in vivo* studies measuring viscoelasticity.

MRI enables representation of the three-dimensional (3D) displacement fields within a volume. By using motion-sensitive gradients, the synchronised, mechanically excited shear waves can be imaged by sampling the waveform at different phases in its cycle. Reconstruction of the elasticity and viscosity can be performed by using a technique (9) that removes dilatational wave contributions, which are difficult to handle because of tissue incompressibility.

The purpose of this work was to investigate viscoelastic properties of normal brain tissue via the full 3D reconstruction method in order to practise the technique for future examination of brain diseases such as hydrocephalus. The *in vivo* MRE results for elasticity and the first measurements of the viscous properties of grey and white matter regions of the brain are presented and compared with previous *in vitro* viscoelastic data.

## THEORY

The MRE technique uses a transducer which transmits vibrations in the tissue of interest, a sequence of

\*Correspondence to: M. A. Green, Prince of Wales Medical Research Institute, Barker St, Randwick, NSW 2031, Australia.  
E-mail: mgreen@unsw.edu.au

**Abbreviations used:** FFT, fast Fourier transform; FOV, field of view; MRE, magnetic resonance elastography.

motion-encoding gradients to image tissue displacement, and a mathematical reconstruction (1,2) to extract mechanical properties of the tissue. A number of different techniques have also been used to reconstruct viscoelastic parameters, which vary depending on the tissue of interest and type of excitation used. Methods range from time-of-arrival technique (14), subzone reconstruction (18), coupled harmonic oscillator simulations (19), and linear (20) and direct (9,21,22) inversion reconstructions.

The harmonic excitation technique used in this study enables reconstruction of viscoelastic parameters by inversion of the Helmholtz equation. The specifics of the technique are described in detail elsewhere (9), but it is worth summarising to distinguish it from other techniques that are similar in their application. An acoustic wave propagating through a locally homogeneous, isotropic, viscoelastic medium is described by the following partial differential equation (23):

$$\rho \partial_t^2 \vec{u} = \mu \nabla^2 \vec{u} + (\lambda + \mu) \nabla (\nabla \cdot \vec{u}) + \eta \partial_t \nabla^2 \vec{u} + (\xi + \eta) \partial_t \nabla (\nabla \cdot \vec{u}) \quad (1)$$

where  $\vec{u}(x, t)$  is the displacement field,  $\rho$  is the density of the medium,  $\mu$  is the shear modulus,  $\lambda$  the second Lamé coefficient,  $\eta$  the shear viscosity and  $\xi$  is the longitudinal viscosity.

The last term on the right hand side of eqn (1) is negligible because the viscosity of the dilatational wave is of small magnitude at the frequencies used here (24) and the nearly incompressible nature of tissue leads to very small values for the  $\nabla(\nabla \cdot \vec{u})$  term. This argument is not applicable to the second term on the right hand side, because  $\lambda$  is of large magnitude, balancing the small magnitude of the  $\nabla(\nabla \cdot \vec{u})$  term, thus creating a so-called pressure term. Eqn (1) can therefore be rewritten as

$$\rho \partial_t^2 \vec{u} = \mu \nabla^2 \vec{u} + \nabla p + \eta \partial_t \nabla^2 \vec{u} \quad , \quad (2)$$

with  $p = \nabla[(\lambda + \mu)\vec{u}]$ , the pressure solely associated with the dilatational wave. The MRE technique below allows one to obtain the displacement field  $\vec{u}(\vec{x}, t)$  within a certain volume. This then enables eqn (2) to become a local inversion problem. A certain proportion of the displacement field consists of dilatational waves created by both the mechanical transducer and shear waves mode-converting at interfaces. Brain tissue is considered to be almost incompressible (25). Thus, there is an enormous imbalance in magnitude between  $\mu$  and  $\lambda$  (about 6 orders of magnitude), which is also reflected in the difference between the speed of the dilatational wave ( $\sim 1550$  m/s) and the speed of the shear wave ( $\sim 1$ – $10$  m/s). This makes the evaluation of dilatational wave contributions very difficult, and the 2<sup>nd</sup> term in eqn (2) is often neglected (14). Dilatational waves form an inevitable part of the excitation in brain elastography, and the curl operator is applied to eqn (2) in order to remove the pressure term (note that the curl of the gradient of a

scalar field is zero). This yields a Helmholtz-type equation and enables reconstruction of the shear viscoelastic parameters  $\mu$  and  $\eta$  with third-order spatial derivatives, i.e. in the case of steady-state excitation  $[\vec{u}(\vec{x}, t) = \vec{u}(\vec{x})e^{i\omega t}]$  at frequency  $\omega$ ,

$$-\rho \omega^2 \vec{q} = \mu \nabla^2 \vec{q} + i\omega \eta \nabla^2 \vec{q} \quad , \quad \vec{q} = \nabla \times \vec{u} \quad (3)$$

More generally, shear stress  $\sigma$  and shear strain  $\varepsilon$  are linked to each other in frequency space by the complex shear modulus  $G^*(\omega)$ , i.e.

$$\sigma(\omega) = G^*(\omega)\varepsilon(\omega) = [G'(\omega) + iG''(\omega)]\varepsilon(\omega) \quad (4)$$

The current measurements obtain storage ( $G'$ ) and loss ( $G''$ ) moduli as the physical parameters extracted from the reconstruction, where  $G'$  and  $G''$  represent the elastic and viscous components of the model, respectively, i.e.  $G' = \mu$ ,  $G'' = \omega\eta$ . Comparison with previous *in vitro* measurements (26–28) is thereby facilitated, as measurements from mechanical rheometers typically provide  $G'$  and  $G''$ .

## EXPERIMENTAL METHOD

The techniques for the scan sequence, theoretical development and reconstruction methods have been described in more detail in previous publications (1,2,9,13). They are outlined here for clarity, as adapted for application to measurement of brain viscoelasticity. A MR-compatible mechanical transducer consisting of two coaxial coils was designed and constructed to be mounted on the transmit/receive Philips 3 T MR-head coil (Fig. 1). The two coils that comprise the transducer are driven by a pulsed signal generator which is triggered by the MR spectrometer. The associated magnetic field created by the coils is coupled with the magnetic field of the MR scanner to produce a torque and the subsequent oscillation of the coils at the determined driving frequency.

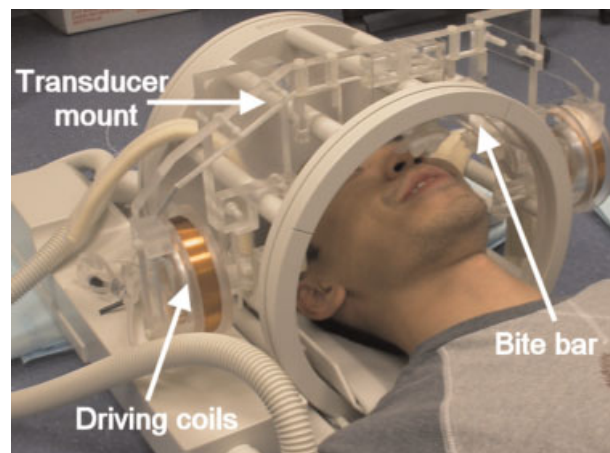


**Figure 1.** MR-compatible transducer mounted on to the transmit/receive Philips MR head coil indicating driving coils and bite bar. This figure is available in colour online at [www.interscience.wiley.com/journal/nbm](http://www.interscience.wiley.com/journal/nbm)

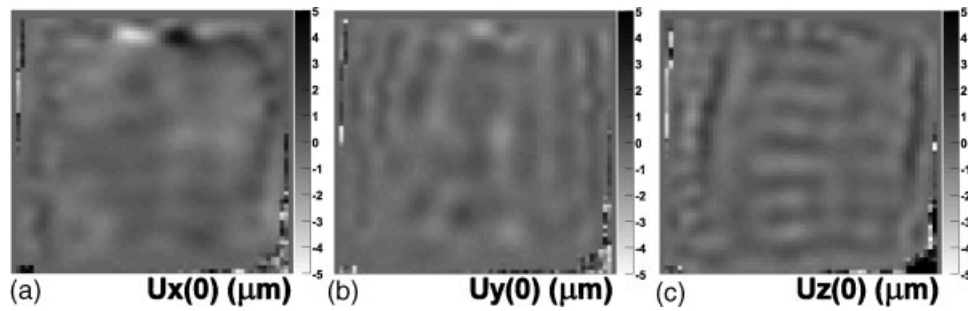


**Figure 2.** Example displacement images for the calibrated phantom ( $\mu\text{m}$ ) at an arbitrary time point  $t_0$  in the  $x$ ,  $y$  and  $z$  directions (a,b and c). The maximum displacement at this particular time point is  $\sim 5 \mu\text{m}$

Reconstruction of the viscoelastic parameters is accomplished using the theory described above. The method of calculating these parameters using the MRE technique has been verified by using a calibrated phantom where values for  $G'$  and  $G''$  were obtained with independent rheometer measurements. The phantom was constructed using oil-in-gelatin dispersions, and, to test a range of viscoelastic properties, inclusions of different consistencies were also placed within the phantom. An excitation frequency value of 200 Hz was chosen in order to match the number of pixels per wavelength for the acquired *in vivo* images ( $\sim 7$  pixels per wavelength). The phantom MRE was performed using a spin-echo sequence with  $TR/TE = 280/30$  ms, four motion-encoding gradients, scan resolution of  $64 \times 64$  pixels, field of view (FOV) = 128 mm, and a 2 mm voxel size. The phantom was held between two plates and vibrated in the head–feet direction. Example wave images at time  $t_0$  in the three imaging directions are shown in Fig. 2 and do not reflect the maximum displacement amplitude. For steady-state elastography, the displacement is described sinusoidally,  $U_i = A_i \sin(\omega t + \varphi_i)$ , where  $i$  describes the three spatial directions,  $A$  is the amplitude,  $\omega$  is the frequency, and  $\varphi$  is the phase. At an arbitrary time point, the displacement field in the different imaging directions can vary, but the amplitude describing the wave will be constant over all time points. The images shown in Fig. 3a,b,c are the associated amplitudes in the three spatial directions. The total amplitude (Fig. 3d) is the square root of the sum of the squares of the amplitudes in each spatial direction. For example, the pixel indicated by the arrow is at the same position within the phantom for each image. The amplitude at this position is 98.3, 66.5 and 43.8  $\mu\text{m}$  for the  $x$ ,  $y$  and  $z$  directions, giving a total amplitude of 126.5  $\mu\text{m}$ .

Figure 4a shows the  $T_2$ -weighted magnitude image indicating the four materials to be reconstructed, an outer layer and an inner layer containing two stiffer inclusions. The reconstructed  $G'$  and  $G''$  images (Fig. 4b,c) show good agreement with the positioning of the inclusions and the boundaries between different media. Sharp boundaries within the phantom result in an estimate of slightly higher viscosity. The MRE values obtained are outlined in

Table 1 alongside previously obtained rheometry measurements (29).

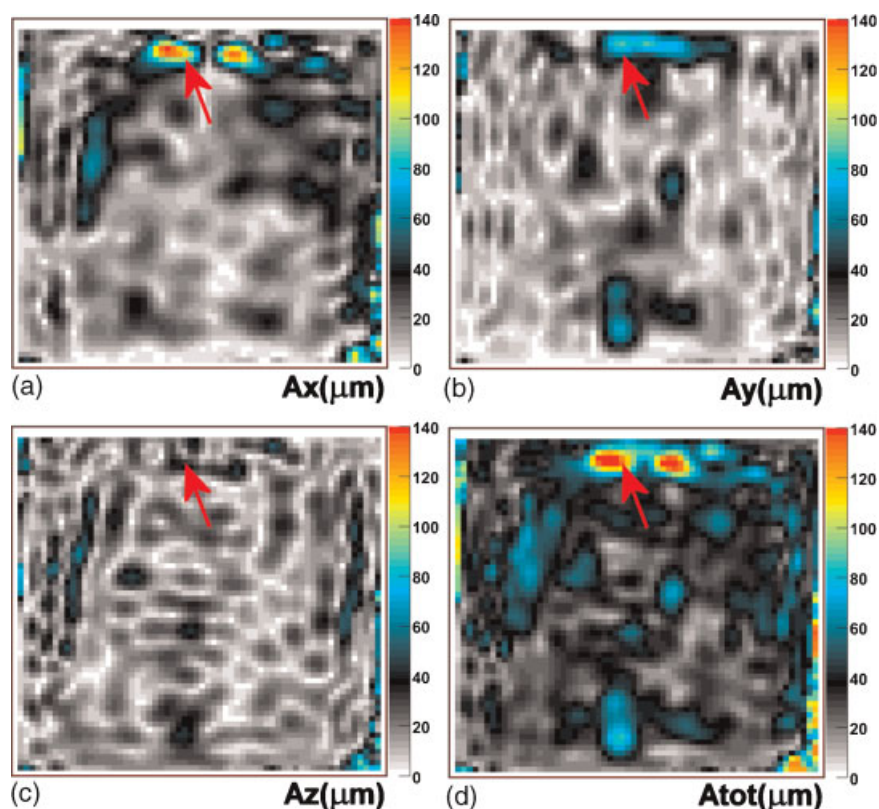
In order to reduce noise, a fast Fourier transform (FFT) filtering process is applied before reconstruction. This filtering process acts as a low-pass filter, and one must therefore be careful that the high spatial frequency waves being excluded are noise and not frequencies of interest. At the centre of the FFT image lie the dilatational wave components, and, as we move radially outwards, higher spatial frequency components lie corresponding to shorter wavelengths. An analysis was undertaken to determine the effect of the filtering on the reconstruction of the viscoelastic parameters by choosing different radial filter cut-offs in frequency space.

To choose a filter for the FFT, we performed a simulation using plane waves (constructed via the Christoffel tensor) within a medium of similar viscoelastic parameters to those of the brain ( $G' = 3.3$  kPa and  $G'' = 1.2$  kPa). The excitation frequency and FOV was also matched to experimental parameters. Figure 5 shows a plot of the difference in the mean value of  $G'$  and  $G''$  from the real value as a function of the FFT filter. It was noted that, above a cut-off value of 85% of the total radial density, there was no significant change in the viscoelastic parameters obtained, and excluded frequencies were thus deemed not to be of interest.

Taking the local magnitude value of the FFT as representative of the importance of the corresponding wave, we calculated the radial density in frequency space of the magnitude values in each direction at an arbitrary time point, and considered the normalised running sum (from the centre towards higher frequencies) of this distribution (Fig. 6a). An examination of the wavelengths in the phantom (Fig. 6b) showed that the smallest wavelengths of interest lie within the softer surrounding materials and were of the order of 12 mm, which corresponds to a radial position in frequency space at 11 pixels (radial pixel position = FOV/wavelength), well within the radial cut-off of 85%, which lies at a radial position of 22 pixels.

The *in vivo* measurements were made using a modified spin-echo pulse sequence (13) using a 3 T MRI scanner (Intera 1.2; Philips Medical Systems, Best,

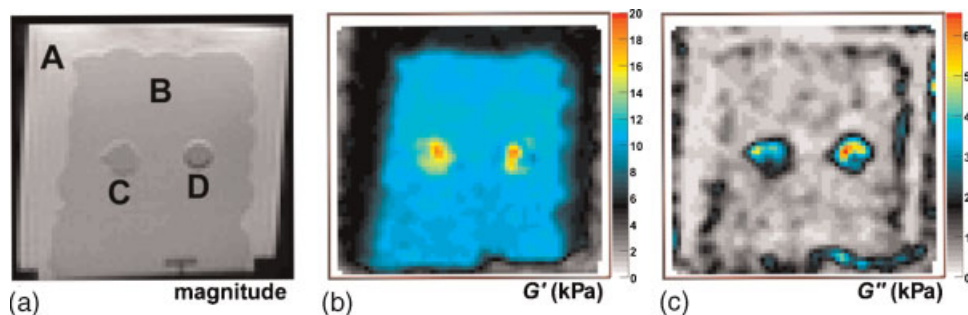




**Figure 3.** (a, b, c) Amplitude images for the three spatial directions  $x$ ,  $y$  and  $z$  ( $\mu\text{m}$ ). The total amplitude (d) is the square root of the sum of the squares of the amplitudes in each spatial direction. This figure is available in colour online at [www.interscience.wiley.com/journal/nbm](http://www.interscience.wiley.com/journal/nbm)

The Netherlands) with a gradient system providing 33 mT/m and 150 mT/m/ms slew rate. Double motion-encoding gradients, which have the same form as the mechanical excitation, are placed before and after the  $\pi$  pulse in the direction of the displacement field to be measured. The amplitude and phase of the 3D displacement field is obtained by imaging the wave field at different phase offsets between the motion-sensitising

gradients and the applied oscillations. The frequency is selected by the frequency generator, and the sinusoidal oscillation drives a bite bar, connected to the driving coils, and transfers this left–right vibration to the skull (and thus the brain) of the test subject (30). A frequency of 90 Hz was used for all *in vivo* data, and typical imaging parameters are  $TR/TE = 550/60$  ms, scan resolution of  $64 \times 64$  pixels,  $FOV = 200$  mm, and slice

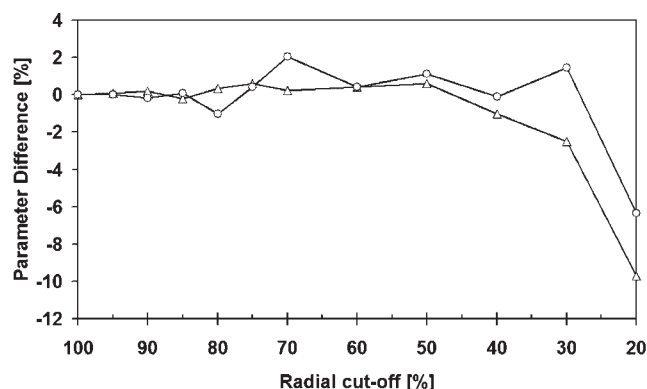


**Figure 4.** Calibrated phantom used to verify the MRE technique and reconstruction. (a) The  $T_2$ -weighted magnitude image shows the four regions of varying viscoelastic parameters. Material A surrounds B, which holds the inclusions C and D. (b, c) The reconstructed  $G'$  and  $G''$  values obtained at an excitation frequency of 200 Hz are shown with the four materials well defined including the stiffer inclusions. This figure is available in colour online at [www.interscience.wiley.com/journal/nbm](http://www.interscience.wiley.com/journal/nbm)

**Table 1.** Measured MRE and previously obtained rheometry measurements (29) for  $G'$  and  $G''$  values for varying viscoelastic properties within the phantom as shown in Fig. 4<sup>a</sup>

Material	MRE		Rheometry (29)	
	$G'$ (kPa)	$G''$ (kPa)	$G'$ (kPa) (50 – 1 Hz)	$G''$ (kPa) (1 – 50 Hz)
A	$6.6 \pm 0.1$	$0.3 \pm 0.1$	$5.1\text{--}6.7 \pm 0.2$	$0.5\text{--}1.9 \pm 0.1$
B	$12.0 \pm 0.6$	$0.7 \pm 0.2$	$10.8\text{--}14.2 \pm 0.7$	$0.9\text{--}1.5 \pm 0.2$
C	$16.2 \pm 1.7$	$3.8 \pm 1.1$	$19.7\text{--}24.2 \pm 2.3$	$1.3\text{--}2.4 \pm 0.4$
D	$23.0 \pm 1.2$	$3.6 \pm 1.2$	$30.6\text{--}33.2 \pm 0.8$	$1.4\text{--}3.2 \pm 0.2$

<sup>a</sup>Values are mean  $\pm$  SD. Rheometry measurements were undertaken at two different frequencies (1 and 50 Hz) in the previous study which accounts for the range of values given.

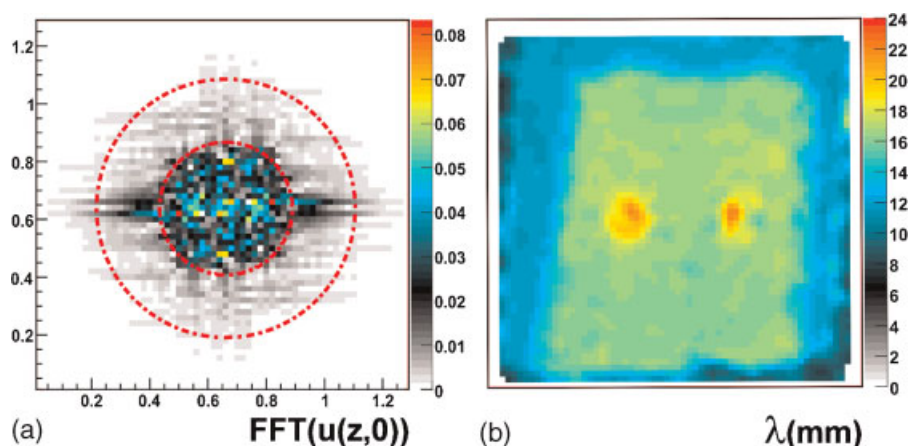
**Figure 5.** Simulated data showing difference between real and reconstructed  $G'$  (triangles) and  $G''$  (circles) values as a function of radial FFT cut-off.

thickness = 3 mm. Measurements consisted of seven slices and eight time offsets leading to a total acquisition time for each dataset of  $\sim 14$  min.

The measurements were obtained while the test subject was in the supine position. The test subjects (five men,

23–61 years of age) were fitted with a sports mouthguard, which was then inserted into the bite bar and vibrated in the axial plane causing mechanical waves to travel via the mandible to the cranium and then into the brain. Displacement field images (see Fig. 8) show that the waves arise coherently from the periphery of the brain towards the centre, indicating that it is caused by vibration of the cranium. However, there may be some inertial effects from the jaw and skull moving as a rigid body contributing to the source of the motion. Informed consent was obtained from each of the healthy volunteers before they entered the scanner, and the protocol was approved by the UNSW Human Research Ethics Committee.

In addition to the MRE dataset, a  $T_2$ -weighted anatomical scan with identical geometry but of higher resolution was also collected to be used to distinguish between white and grey matter when extracting viscoelastic parameters. The *in vivo* datasets were then reconstructed to obtain images for the analysis as described above. Regions of interest in grey and white matter were manually selected within each representation

**Figure 6.** (a) An example FFT image of the displacement field  $[u(z,0)]$  in the  $z$  direction at an arbitrary time point ( $t_0$ ) using an 85% radial cut-off filter (outer dotted circle). The inner circle indicates a radial position of 11 pixels corresponding to the smallest wavelengths of interest. (b) An image map of the wavelengths within the different regions of the phantom. Wavelengths range from  $\sim 10$  mm in the outer region of the phantom to 22 mm in the inclusions. This figure is available in colour online at [www.interscience.wiley.com/journal/nbm](http://www.interscience.wiley.com/journal/nbm)

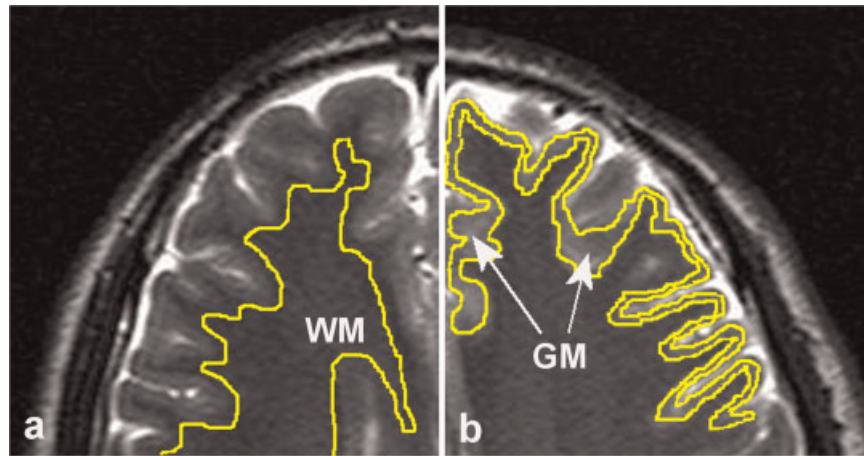


**Figure 7.** An example magnified  $T_2$ -weighted image showing the regions of interest selected for viscoelastic property measurements in (a) white matter (WM) and (b) grey matter (GM). This figure is available in colour online at [www.interscience.wiley.com/journal/nbm](http://www.interscience.wiley.com/journal/nbm)

with Image J processing software (<http://rsb.info.nih.gov/ij/>) to provide a mean value for each test subject and each viscoelastic parameter. An example image indicating the grey and white matter regions magnified for clarity is shown in Fig. 7.

## RESULTS

Data were collected in the axial plane with the slices in the region of the brain located within and just above the ventricles. Example shear wave images in black and white

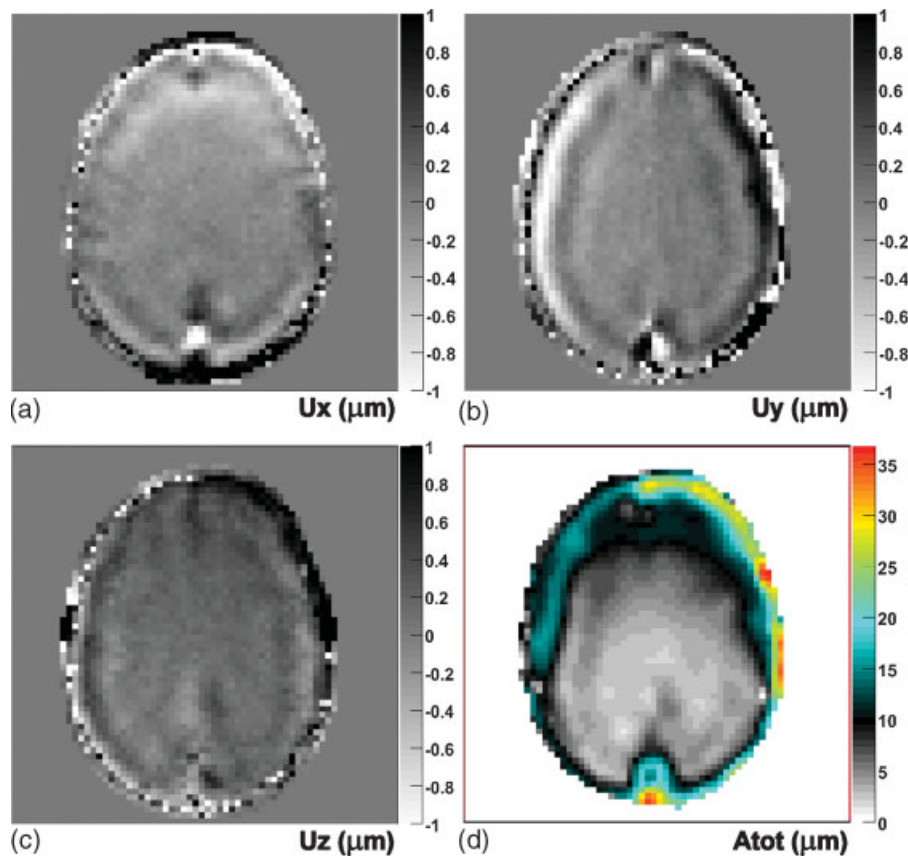


**Figure 8.** An example of the measured displacement field components in the  $x$ ,  $y$  and  $z$  directions (a, b and c) in micrometres at an arbitrary time point for an *in vivo* dataset. The total amplitude image (d) indicates the strong attenuation occurring within the brain as the shear waves move towards its centre.



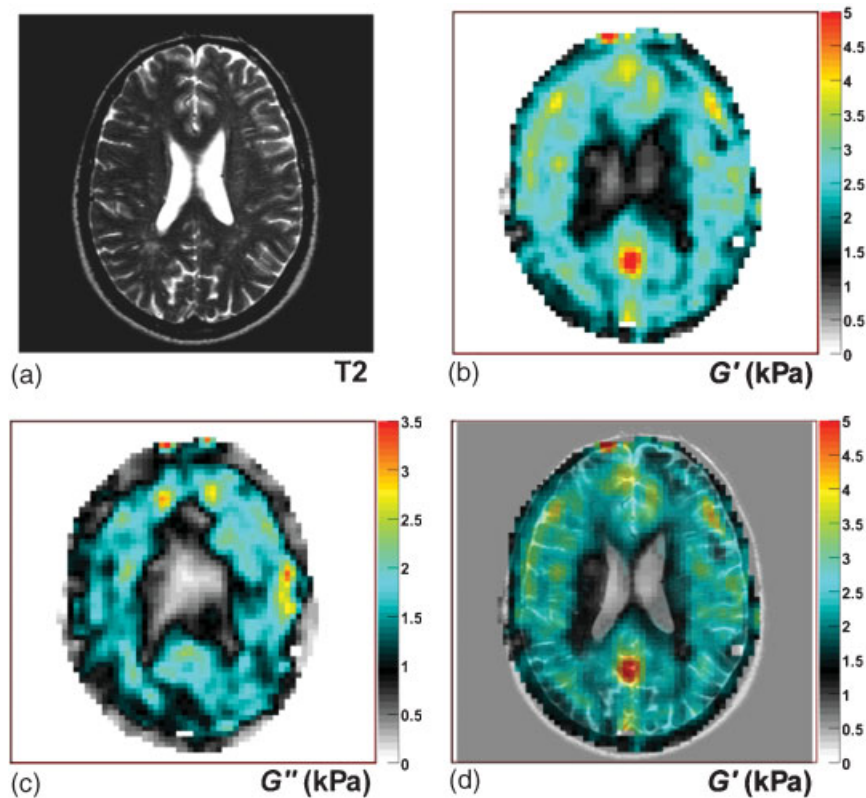


**Figure 9.** An example of an *in vivo* reconstruction. (a)  $T_2$ -weighted MR image; (b)  $G'$  (kPa) image; (c)  $G''$  (kPa) image. Elasticity overlaid with the  $T_2$ -weighted image is shown in (d). Ventricles in the region of low elasticity are visible in the centre of the image.

(Fig. 8a,b,c) are the  $x$ ,  $y$  and  $z$  components of the measured displacement field for an arbitrary time point  $t_0$  during the oscillatory cycle. The amplitudes are in micrometres and are at a maximum around the perimeter of the skull where shear wave excitation begins. The attenuation of shear waves toward the centre of the brain is evident in these images and quantified further in Fig. 8d, where the total amplitude for the complex value displacement vector  $\vec{u}$  is shown. The amplitude near the cranium is of the order of  $30\ \mu\text{m}$ , whereas typical values at the centre of the brain are of the order of  $2 - 5\ \mu\text{m}$ .

Figure 9a shows a  $T_2$ -weighted MR-magnitude image. Reconstructed maps for the storage modulus  $G'$  and the loss modulus  $G''$  are shown in Fig. 9b,c. In addition, Fig. 9d shows a  $T_2$ -weighted magnitude image overlaid with the elasticity reconstruction for convenience. The elasticity image indicates higher values around the outside of the image decreasing towards the centre, where there is a clear decrease in the region of the ventricles. A similar decrease in viscosity seen in the central part of the image is also shown in Fig. 9c, but there is no significant difference between values obtained for grey and white matter. The compiled results of the *in vivo* measurements from five volunteers are presented in Table 2 where a value for elasticity and viscosity for grey matter and white matter is given. The measurements

yielded mean  $\pm$  standard error values for grey and white matter storage modulus of  $3.1 \pm 0.1\ \text{kPa}$  and  $2.7 \pm 0.1\ \text{kPa}$ , respectively, and the corresponding values for the loss modulus are  $2.5 \pm 0.2\ \text{kPa}$  for grey matter and  $2.5 \pm 0.2\ \text{kPa}$  for white matter. The measurements obtained for each of the five subjects were subjected to a paired  $t$ -test for grey and white matter elasticity, and

**Table 2.** *In vivo* measurements of viscoelastic parameters for grey and white matter for five volunteers<sup>a</sup>

Subject	$G'$ (kPa)		$G''$ (kPa)	
	Grey	White	Grey	White
A	$3.4 \pm 0.8$	$2.6 \pm 0.8$	$2.6 \pm 1.0$	$1.9 \pm 1.0$
B	$3.4 \pm 0.5$	$3.4 \pm 0.5$	$2.5 \pm 0.8$	$3.2 \pm 0.9$
C	$3.6 \pm 0.9$	$3.3 \pm 0.5$	$2.4 \pm 1.0$	$2.9 \pm 0.8$
D	$2.9 \pm 0.4$	$2.3 \pm 0.5$	$2.5 \pm 1.1$	$2.2 \pm 0.9$
E	$2.3 \pm 0.7$	$1.7 \pm 0.5$	$2.4 \pm 1.0$	$2.4 \pm 0.8$
Mean	$3.1 \pm 0.1$	$2.7 \pm 0.1$	$2.5 \pm 0.2$	$2.5 \pm 0.2$

<sup>a</sup>Values are mean  $\pm$  standard error. Mean  $G'$  values for grey (3.1 kPa) and white (2.7 kPa) matter are significantly different ( $P=0.02$ ), whereas the mean  $G''$  values for grey (2.5 kPa) and white (2.5 kPa) matter are not significantly different. A paired  $t$ -test on the standard deviations for each subject does not reveal any significance that would affect the significance between grey and white matter values.

the difference was found to be statistically significant ( $P=0.02$ ). The same test applied to the standard deviations for each subject did not show any significance and therefore they do not affect the significance of the difference in grey and white matter elasticity. There was no significant difference in loss modulus values between grey and white matter.

## DISCUSSION

Reconstruction of the storage modulus  $G'$  and the loss modulus  $G''$  utilises the technique described in (9). The reconstruction relies on the assumption that the tissue is isotropic, but it is known that white brain matter is anisotropic. An increase in excitation frequency would enable better spatial resolution and perhaps an insight into the anisotropic nature of white matter. However, attenuation of the shear waves increases with frequency, particularly affecting wave amplitude in deep regions of the brain. Further work will endeavour to probe anisotropy of the brain using MRE, but this is a limitation of the current results. The reconstruction used here is also sensitive to noise because of the use of third-order derivative calculations, arising from application of the curl operator, as has been highlighted and discussed previously (9).

The calibrated phantom demonstrates the performance of the reconstruction method by providing good agreement between the values obtained via the MRE technique and the rheometry measurements for the different viscoelastic materials. The measurements for the larger surrounding regions compare very favourably with the rheometry data. Some discrepancies exist for the smaller, stiffer inclusions and indeed the difference becomes larger for the much stiffer materials C and D. This may be attributed to (a) the excitation frequency being too low to provide enough wavelengths inside the inclusion and (b) partial-volume effects occurring at inclusion boundary interfaces. This may also be the cause of any heterogeneity, but may also be due to imperfections within the inclusion or low spatial resolution. The  $G'$  rheometry measurements decreased with increasing frequency, and the  $G''$  values increased. Although there are insufficient data to extrapolate these parameters with any certainty, the trend may see the elasticity and the viscosity values nearer those obtained at 200 Hz used for the MRE experiments. Analysis of the calibrated phantom using different FFT filter specifications confirmed that filtering did not play any significant role in the underestimation of the inclusion properties. Future experiments that endeavour to reconstruct viscoelastic properties of materials or tissues that are less stiff than those reported here must be careful to ensure that the FFT filtering method is not excluding high frequencies, which could potentially underestimate the elasticity.

**Table 3.** *In vivo* storage and loss modulus quantities for grey and white matter regions of the brain for healthy volunteers after region of interest analysis at 90 Hz as obtained by the MRE method in this analysis. Comparisons with previously published MRE and *in vitro* measurements are also given

	$\omega$ (Hz)	$G'$ (kPa)	$G''$ (kPa)
<i>Grey matter</i>			
Human MRE – present data	90	$3.1 \pm 0.1$	$2.5 \pm 0.2$
Human MRE – McCracken (14)	80	$5.3 \pm 1.3$	
Human MRE – Uffmann (31)	83	12.9	
Bovine <i>in vitro</i> – Darvish (28)	90	$\sim 3.5$	$\sim 2.0$
<i>White matter</i>			
Human MRE – present data	90	$2.7 \pm 0.1$	$2.5 \pm 0.2$
Human MRE – McCracken (14)	80	$10.7 \pm 1.4$	
Human MRE – Uffmann (31)	83	15.2	
Bovine <i>in vitro</i> – Bilston (26)	10	$\sim 5.0$	$\sim 0.6$
Porcine <i>in vitro</i> – Nicolle (27)	90	3.5–7.5	2.7–5.3
<i>Brain matter</i>			
Human MRE – Hamhaber (15)	83	3.5	

The *in vivo* measurements are compared with storage and loss moduli ( $G'$  and  $G''$ ) measurements from previous studies of brain matter using various techniques and models in Table 3. There are only a few studies that have obtained grey and white matter values concurrently (14,31), including the present data, and therefore they are the only measurements where one should compare grey and white matter magnitudes. Viscoelastic characterisation will vary as a function of frequency, as shown previously for canine liver tissue (32) for example, so results will differ for different MRE excitation frequencies. Rheometry measurements (26) for bovine white matter brain tissue *in vitro* have been made previously, and values of  $G' \sim 5$  kPa and  $G'' \sim 0.6$  kPa were obtained at 10 Hz, much lower than the 90 Hz excitation used for MRE. The values obtained for  $G''$  in (26) show a trend towards lower values for higher frequencies, and the elasticity values appear to be flattening out towards higher frequencies. Recent rheological *in vitro* measurements on porcine white matter brain tissue (27) have reported  $G'$  values in the range 3.5–7.5 kPa and  $G''$  values in the range 2.7–5.3 kPa at 90 Hz. Elasticity values have also been obtained for bovine grey matter tissue *in vitro* (28). That analysis used measurements in the frequency range 1–100 Hz, and values of  $G' \sim 3.5$  kPa and  $G'' \sim 2.0$  kPa were found at 90 Hz.

The previous human brain MRE measurements *in vivo* of McCracken *et al.* (14) and Hamhaber *et al.* (15) used different methods to analyse experimental data to extract elastic properties of brain tissue. Differences between those results and this study may be explained by considering the reconstruction of the central region of the brain, where amplitudes become small. The central ventricular region has emerged in the images as an area of



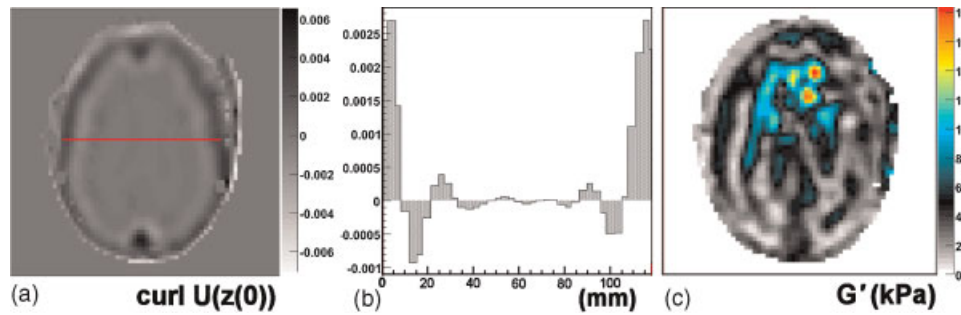


**Figure 10.** (a) An image of the  $z$  component of the rotation at time  $t_0$  of the displacement field  $\{\text{curl } U[z(0)]$ , no units. The horizontal line indicates the length (mm) used for the line profile (b) showing the decrease across the centre despite the large overall wave amplitude still present. (c) Reconstructed map of shear elasticity without application of the curl operator, i.e. inverting eqn (2) and ignoring the pressure term. This figure is available in colour online at [www.interscience.wiley.com/journal/nbm](http://www.interscience.wiley.com/journal/nbm)

low  $G'$  and  $G''$ , as expected for cerebrospinal fluid (33). Cerebrospinal fluid in the ventricles is a nearly Newtonian viscous fluid, with viscosity of  $\sim 0.7\text{--}1\text{ mPa}\cdot\text{s}$  (33). This leads to a nearly zero elasticity and a  $G'' (= \omega\eta \sim 0.5\text{ kPa})$  that is much lower than the surrounding brain tissue. Although this is consistent with what we have observed, this result should be viewed with caution, because we have low signal in this region because of attenuation of the shear waves deep in the brain, there may be partial-volume effects at the border of the ventricles due to the limited spatial resolution, and the model has not been verified for materials with viscoelastic behaviour that is dominated by fluid rather than solid characteristics. A reconstruction without application of the curl operator to an example brain dataset can be considered as shown in Fig. 10. Figure 10a shows an image map of the rotation in the  $z$  direction (no units) at an arbitrary time point  $t_0$ , and a horizontal line (mm) is drawn to plot a line profile (Fig. 10b). It indicates low amplitudes in the central region, but reconstruction without application of the curl operator leads to an overestimation of elasticity in the central area (Fig. 10c). Thus, one would find that white matter is stiffer than grey matter, which is opposite to the findings when the curl operator was used. This might explain the difference between the values obtained in this analysis and previous MRE measurements (14) that showed increased stiffness around the area of the ventricles.

The MRE reconstruction technique has been verified via rheometry measurements on a calibrated phantom, and although it correctly predicts these values, further investigations (with phantoms resembling the subtle variations in brain structure or detailed simulations for example) are needed to place limitations on its sensitivity. Regions of interest in the brain were selected from the  $T_2$  anatomical image in order to avoid grey and white matter boundaries. However, it is also important to note that this does not completely exclude the possibility of error due to partial-volume effects. The robustness of the reconstruction is also correlated with the signal-to-noise ratio of the

image acquisition, and additional investigation into this relationship is required.

Interestingly, all *in vivo* measurements and images have revealed an area of increased elasticity posterior to the corpus callosum, which can be identified in Fig. 9b,d, giving an elasticity value of  $\sim 5\text{ kPa}$ . The reconstruction technique takes the curl of the displacement field, removing dilatational waves and thus removing other sources of motion within the brain itself, so we can eliminate this as a possible cause for the increase in elasticity. The region may lie within the posterior cingulate gyrus, as it appears to be superior to the area about the great cerebral vein of Galen. Further investigations may assist in analysing this result, but it may be that the vasculature plays a role in this region.

The objective of this work was to provide additional experimental data, particularly viscoelastic properties for the human brain *in vivo*, and to demonstrate the strengths and weaknesses of this technique for brain application. The phantom data confirmed the validity of the MRE technique and verified the reconstruction and its associated filtering method. The *in vivo* brain measurements imparted further elasticity data as well as the first *in vivo* loss modulus datasets. Moreover, the values obtained for  $G'$  and  $G''$  agree well with *in vitro* brain data published elsewhere. Further phantom and reconstruction techniques need to be pursued to investigate the differences in magnitude with previous MRE measurements, but this study indicates that the methodology is now robust enough to begin to explore using it for *in vivo* measurements in patients with brain diseases such as hydrocephalus and tumours.

## Acknowledgements

We thank members of the Magnetic Resonance Laboratory at the Mayo Clinic, particularly Richard Ehman for his correspondence and valuable assistance, as well as the Australian Research Council (ARC) for project funding.

## REFERENCES

- Muthupillai R, Rossman PJ, Lomas DJ, Greenleaf JF, Riederer SJ, Ehman RL. Magnetic resonance imaging of transverse acoustic strain waves. *Magn Reson Med* 1996; **36**: 266–274.
- Muthupillai R, Lomas DJ, Rossman PJ, Greenleaf JF, Manduca A, Ehman RL. Magnetic resonance elastography by direct visualization of propagating acoustic strain waves. *Science* 1995; **269**: 1854–1857.
- Catheline S, Wu F, Fink M. A solution to diffraction biases in sonoelasticity: the acoustic impulse technique. *J. Acoust Soc Am* 1999; **105**: 2941–2950.
- Yamakoshi Y, Sato J, Sato T. Ultrasonic imaging of internal vibration of soft tissue under forced vibration. *IEEE Transactions on Ultrasonics, Ferroelectrics and Frequency Control* 1990; **37**: 45–53.
- Lerner RM, Huang SR, Parker KJ. “Sonoelasticity” images derived from ultrasound signals in mechanically vibrated tissues. *Ultrasound Med Biol* 1990; **16**: 231–239.
- Parker KJ, Lerner RM. Sonoelasticity of organs: shear waves ring a bell. *J. Ultrasound Med* 1992; **11**: 387–392.
- Sinkus R, Tanter M, Catheline S, Lorenzen J, Kuhl C, Sondermann E, Fink M. Imaging anisotropic and viscous properties of breast tissue by magnetic resonance-elastography. *Magn Reson Med* 2005; **53**: 372–387.
- McKnight AL, Kugel JL, Rossman PJ, Manduca A, Hartmann LC, Ehman RL. MR elastography of breast cancer: preliminary results. *AJR Am J Roentgenol* 2002; **178**: 1411–1417.
- Sinkus R, Tanter M, Xydeas T, Catheline S, Bercoff J, Fink M. Viscoelastic shear properties of *in vivo* breast lesions measured by MR elastography. *Magn Reson Imaging* 2005; **23**: 159–165.
- Kemper J, Sinkus R, Lorenzen J, Nolte-Ernsting C, Stork A, Adam G. MR elastography of the prostate: initial in-vivo application. *Rofo* 2004; **176**: 1094–1099.
- Uffmann K, Maderwald S, Ajaj W, Galban CG, Mateiescu S, Quick HH, Ladd ME. *In vivo* elasticity measurements of extremity skeletal muscle with MR elastography. *NMR Biomed* 2004; **17**: 181–190.
- Dresner MA, Rose GH, Rossman PJ, Muthupillai R, Manduca A, Ehman RL. Magnetic resonance elastography of skeletal muscle. *J. Magn Reson Imaging* 2001; **13**: 269–276.
- Sinkus R, Lorenzen J, Schrader D, Lorenzen M, Dargatz M, Holz D. High-resolution tensor MR elastography for breast tumour detection. *Phys Med Biol* 2000; **45**: 1649–1664.
- McCracken PJ, Manduca A, Felmlee J, Ehman RL. Mechanical transient-based magnetic resonance elastography. *Magn Reson Med* 2005; **53**: 628–639.
- Hamhaber U, Sack I, Papazoglou S, Rump J, Klatt D, Braun J. Three-dimensional analysis of shear wave propagation observed by *in vivo* magnetic resonance elastography of the brain. *Acta Biomater* 2007; **3**: 127–137.
- Xu L, Lin Y, Xi ZN, Shen H, Gao PY. Magnetic resonance elastography of the human brain: a preliminary study. *Acta Radiol* 2007; **48**: 112–115.
- Xu L, Lin Y, Han JC, Xi ZN, Shen H, Gao PY. Magnetic resonance elastography of brain tumors: preliminary results. *Acta Radiol* 2007; **48**: 327–330.
- Van Houten EE, Doyle MM, Kennedy FE, Weaver JB, Paulsen KD. Initial *in vivo* experience with steady-state subzone-based MR elastography of the human breast. *J. Magn Reson Imaging* 2003; **17**: 72–85.
- Sack I, Bernarding J, Braun J. Analysis of wave patterns in MR elastography of skeletal muscle using coupled harmonic oscillator simulations. *Magn Reson Imaging* 2002; **20**: 95–104.
- Bishop J, Samani A, Sciarretta J, Plewes DB. Two-dimensional MR elastography with linear inversion reconstruction: methodology and noise analysis. *Phys Med Biol* 2000; **45**: 2081–2091.
- Oliphant TE, Manduca A, Ehman RL, Greenleaf JF. Complex-valued stiffness reconstruction for magnetic resonance elastography by algebraic inversion of the differential equation. *Magn Reson Med* 2001; **45**: 299–310.
- Plewes DB, Bishop J, Samani A, Sciarretta J. Visualization and quantification of breast cancer biomechanical properties with magnetic resonance elastography. *Phys Med Biol* 2000; **45**: 1591–1610.
- Landau LD, Lifschitz EM. *Theory of Elasticity*. Pergamon Press: New York, 1986.
- Kinsler L. *Fundamentals of Acoustics*. New York: John Wiley & Sons: 1982.
- Franceschini G, Bigoni D, Regitnig P, Holzapfel GA. Brain tissue deforms similarly to filled elastomers and follows consolidation theory. *Journal of Mechanics and Physics of Solids* 2006; **54**: 2592–2620.
- Bilston LE, Liu Z, Phan-Thien N. Large strain behaviour of brain tissue in shear: some experimental data and differential constitutive model. *Biorheology* 2001; **38**: 335–345.
- Nicolle S, Lounis M, Willinger R, Paliere JF. Shear linear behavior of brain tissue over a large frequency range. *Biorheology* 2005; **42**: 209–223.
- Darvish KK, Crandall JR. Nonlinear viscoelastic effects in oscillatory shear deformation of brain tissue. *Med Eng Phys* 2001; **23**: 633–645.
- Madsen EL, Hobson MA, Frank GR, Shi H, Jiang J, Hall TJ, Varghese T, Doyle MM, Weaver JB. Anthropomorphic breast phantoms for testing elastography systems. *Ultrasound Med Biol* 2006; **32**: 857–874.
- Kruse S, Dresner M, Rossman P, Felmlee J, Jack C, Ehman R. Palpation of the brain using magnetic resonance elastography. Proceedings of the 7th Annual Meeting of ISMRM, Philadelphia, 1999; 258.
- Uffmann K, Maderwald S, de Greiff A, Ladd ME. Determination of gray and white matter elasticity with MR elastography. ISMRM Proceedings, Kyoto, 2004; 1768.
- Kiss MZ, Varghese T, Hall TJ. Viscoelastic characterization of *in vitro* canine tissue. *Phys Med Biol* 2004; **49**: 4207–4218.
- Bloomfield IG, Johnston IH, Bilston LE. Effects of proteins, blood cells and glucose on the viscosity of cerebrospinal fluid. *Pediatr Neurosurg* 1998; **28**: 246–251.